

Chapter Six: Comparison of Turbulence Models

Performance Comparisons

There are a number of criteria by which to judge turbulence models. One criterion sometimes important to mathematically-minded model developers is the consistency and accuracy of the mathematics involved in the derivation of a model. A similar criterion is the belief that the best turbulence model is the one that correctly models the most and most fundamental physics of turbulence itself. Such criteria have been briefly discussed in Chapter Three. Another approach to turbulence modeling looks solely at the solutions generated using a given turbulence model and compares the solutions to those generated by others and to experimental data. According to this line of reasoning, the best turbulence model is simply the one that best matches the experimental data, no matter what its origin. Still another approach concerns itself with a quality per unit cost ratio, considering that an accurate but computationally expensive turbulence model might be less useful than a slightly less accurate, inexpensive one. In the present section the turbulence models used in this study will be examined from a number of these points of view.

Turbulence Model Comparisons

A reasonable beginning in the comparison of two or more turbulence models is a simple examination of the results they produce, with attention to the similarities and differences in the solutions. To that end the following pages will compare the RNG and Chien $K-\epsilon$ solutions to all three test problems, the flat plate, the nine-hole array injector, and the four-hole ramp injector.

Flat-Plate

As stated earlier, the purpose of the flat-plate study was to create an opportunity for side-by-side comparison of “fast” RNG and

Chien $K-\epsilon$ under completely identical conditions. “Mixing” RNG was not compared because for a single-species problem it reduces to “fast” RNG.

Perhaps the most efficient means of presenting boundary-layer data is the line plot, used in the previous chapter for this purpose. Figures 6.1 through 6.4 present profiles of velocity, static temperature, static density, turbulent viscosity ratio in a single plane, $x=1.00$ m from the leading edge. Notice that in every figure the “fast” RNG result is indistinguishable from the Chien $K-\epsilon$. These results suggest that for a relatively simple case such as supersonic flow over a flat plate there are no discernible differences whatsoever between solutions generated by a Chien $K-\epsilon$ turbulence model and solutions generated by the “fast” RNG model. Because RNG $K-\epsilon$ is merely a higher-order correction to the standard model, differences should not be expected in flows where the correlation of velocity gradients are weak, or in situations where the standard model generally performs well. For both these reasons, RNG $K-\epsilon$ is expected to return a very similar answer to that of the Chien $K-\epsilon$ model in this case. The issue of agreement with theory will be addressed in a later section.

Wall Injector Array

Figures 6.5 through 6.7 show helium mass-fraction contours for the fine-mesh solutions for all turbulence models on three different planes, the centerplane in the injector region, one nearfield crossflow plane, six effective diameters downstream from the origin, and the crossflow plane at the measurement station, forty-three effective diameters downstream from the center of the first row of injectors. The origin is again at the center of the first row of injectors. Note that in these and following figures the coordinate axes and contour data are plotted on different scales at the measurement station than they are in nearfield plots. In each of these planes the injectant distributions are clearly very similar, regardless of turbulence model. Whatever influence the RNG $K-\epsilon$ models have upon the flowfield is

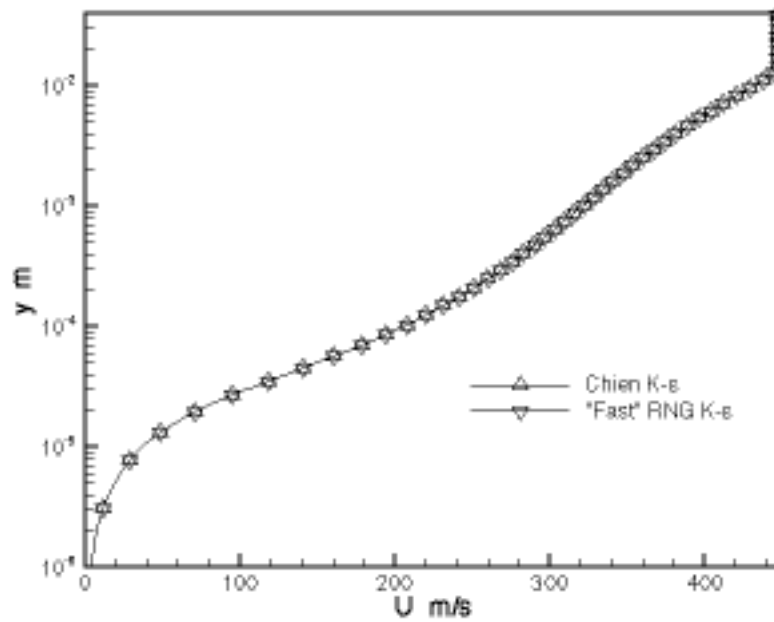


Figure 6.1. Streamwise Velocity as a Function of Normal Distance for the Flat Plate Test Case at $x=1.00$ m. Every Fourth Point Is Marked.

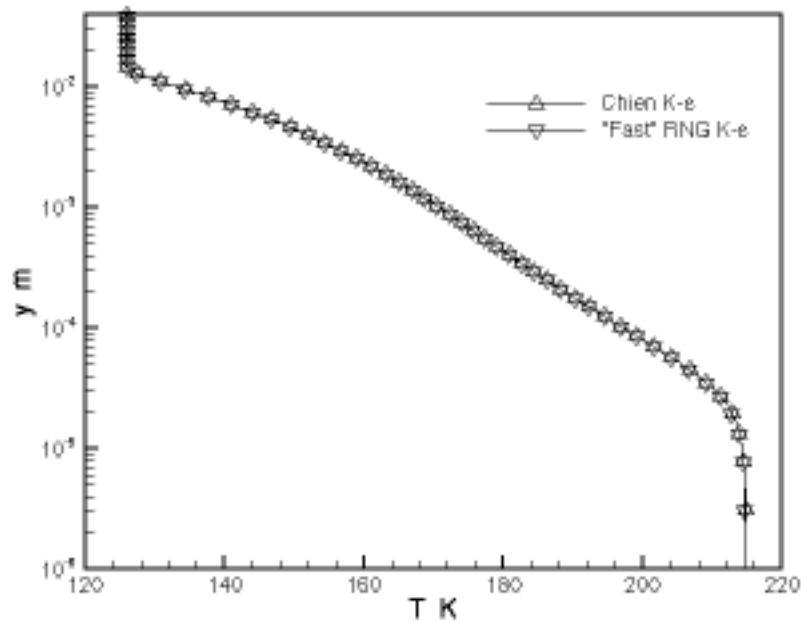


Figure 6.2. Static Temperature as a Function of Normal Distance for the Flat Plate Test Case at $x=1.00$ m. Every Fourth Point Is Marked.

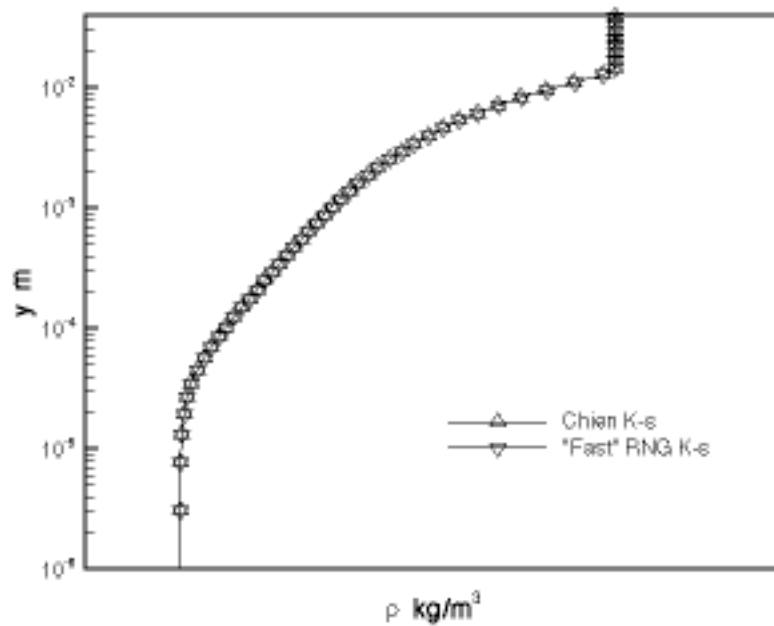


Figure 6.3. Static Density as a Function of Normal Distance for the Flat Plate Test Case at $x=1.00$ m. Every Fourth Point Is Marked.

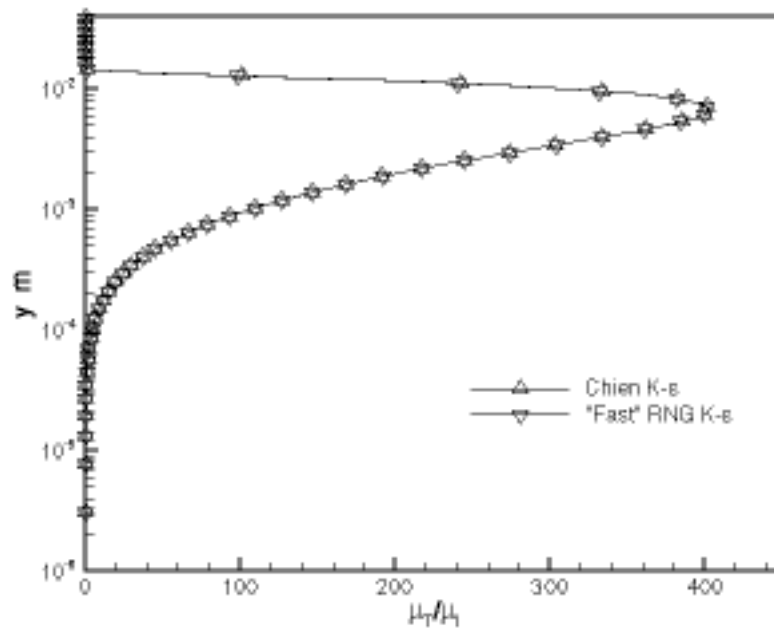


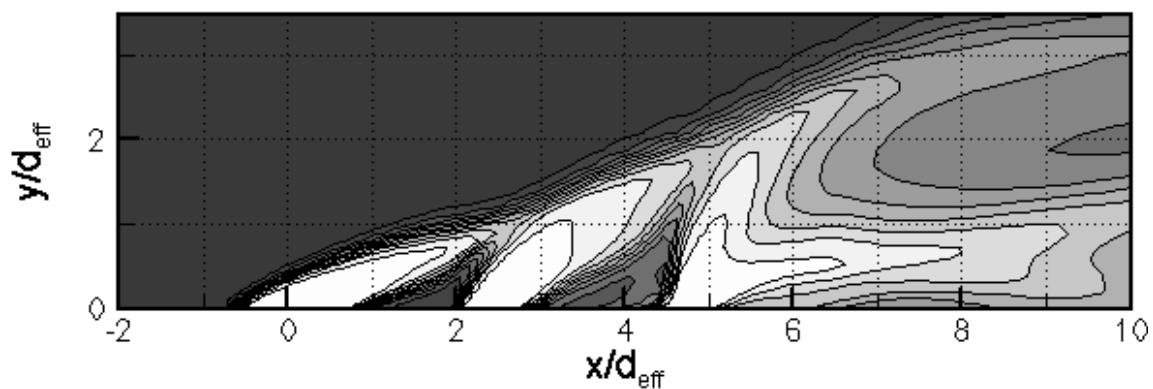
Figure 6.4. Turbulent (Eddy) Viscosity Ratio as a Function of Normal Distance for the Flat Plate Test Case at $x=1.00$ m. Every Fourth Point Is Marked.

reflected only very weakly in mixing data; even the "mixing" RNG solution appears virtually indistinguishable from the other two. Figures 6.8 through 6.10 show pressure data at the same locations, and Figures 6.11 through 6.13 show Mach number data. In each of these figures the conclusion is the same: the RNG variations of $K-\epsilon$ implemented in this study have not made an appreciable difference in the computed flow solution for the mean-flow variables.

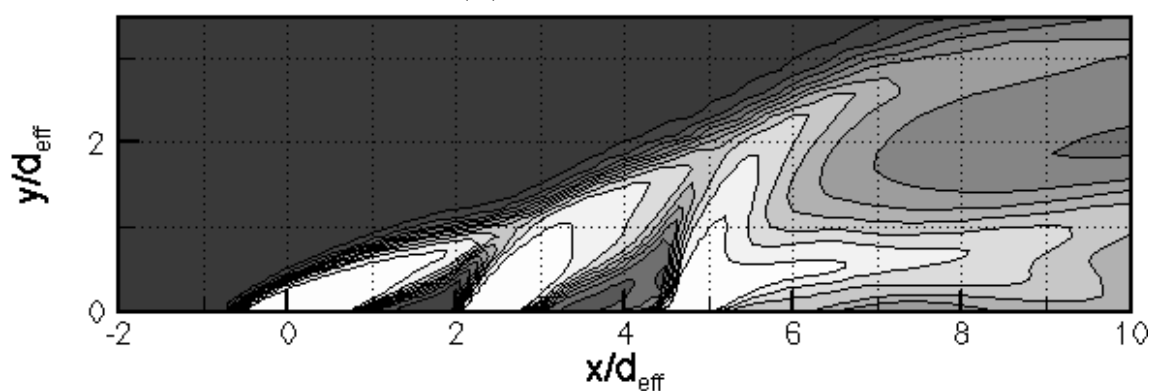
There are at least two possible explanations for this lack of impact. The simplest is to suggest that the RNG additions to the $K-\epsilon$ turbulence model do not significantly impact the solution in this flow. While this is a reasonable conclusion, acceptance of this conclusion must be tempered by the grid convergence study of the previous chapter, which suggests that, particularly in the farfield region, grid convergence has not been achieved in this study. Because grid convergence has not been proven, the possibility exists that one turbulence model or another is better able to predict the flow, but has been prevented from doing so by grid-dependent numerical dissipation. Only calculations on a series of finer meshes would definitively answer the question. The grid convergence study did indicate that the nearfield region was significantly better grid-converged, however the flow in the nearfield region is expected to be dominated by inviscid effects, which would reduce the impact of turbulence and the turbulence model and would result in solutions that are strongly similar regardless of the turbulence treatment.

Ramp Injector

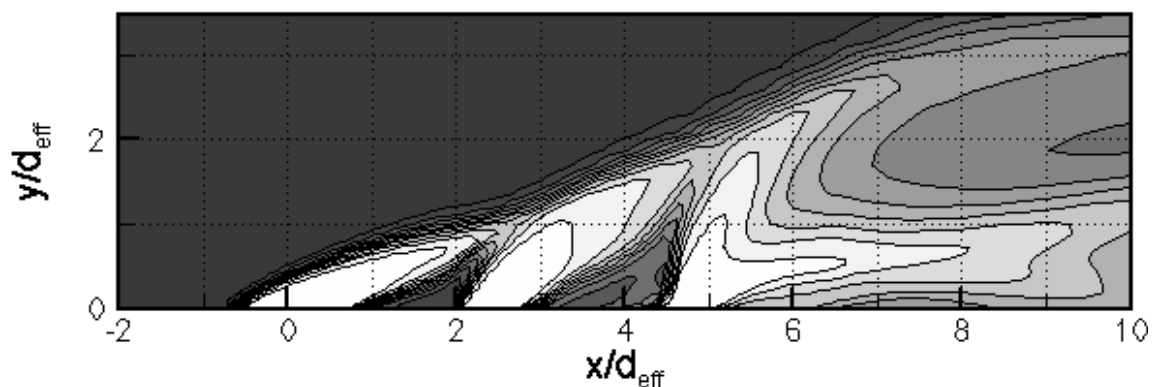
We begin with comparisons of meanflow data. Figures 6.14 through 6.16 present helium mass-fraction data for both turbulence models at three axial stations, $x/h=0.500$, $x/h=2.50$, and $x/h = 20.0$. Figures 6.17 through 6.19 compare the pressure fields at the same locations, and Figures 6.20 through 6.22 compare Mach number. In these figures and those to follow, "mixing" RNG data is on the left and Chien $K-\epsilon$ data is on the right, as a mirror image. ("Fast" RNG $K-\epsilon$ was not employed in this case.) Contour levels for the nearfield data



(a) Chien $K - \epsilon$

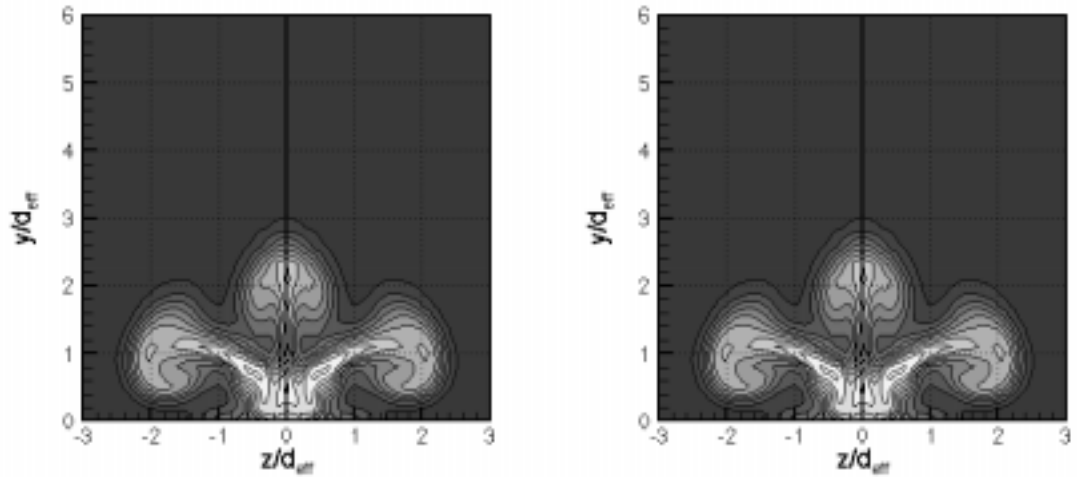


(b) "Fast" $RNGK - \epsilon$



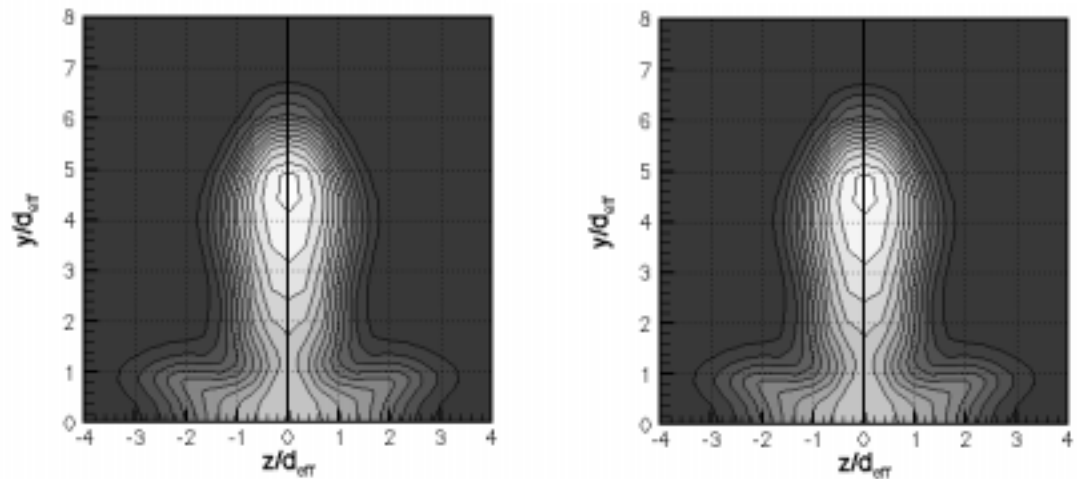
(c) "Mixing" $RNGK - \epsilon$

Figure 6.5. Centerplane Helium Mass-Fraction Contours for Three Turbulence Models for the Nine-Hole Injector Array.



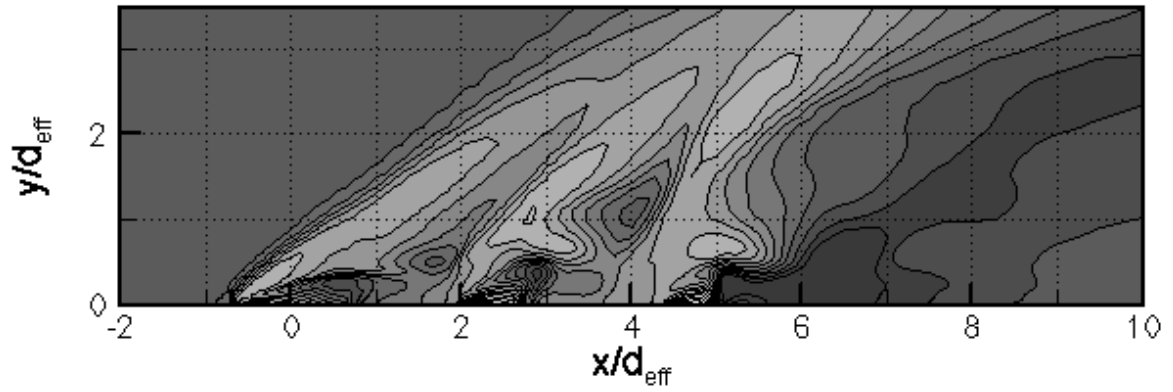
(a) "Fast" RNG (left) and Chien $K - \epsilon$ (b) "Mixing" RNG (left) and Chien $K - \epsilon$

Figure 6.6. Helium Mass-Fraction Contours for Three Turbulence Models on a Spanwise Plane at $x/d_{eff} = 6.00$ for the Nine-Hole Injector Array.

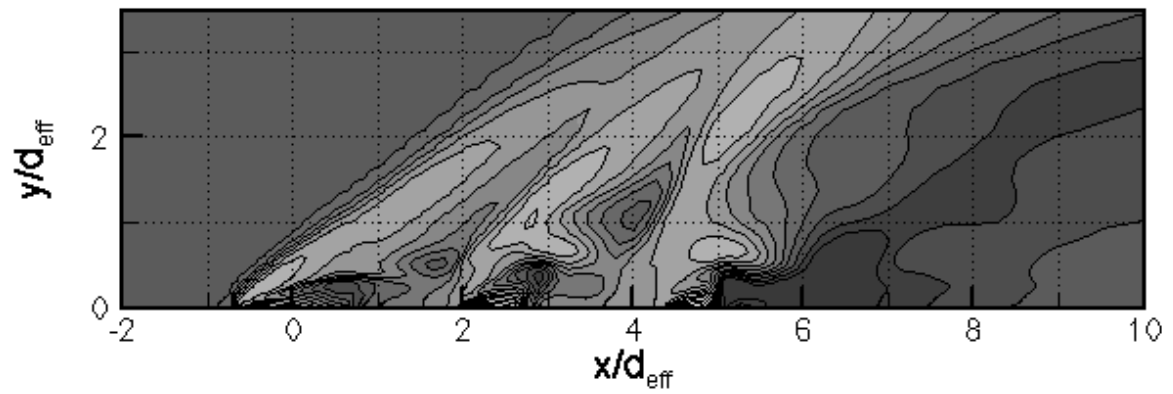


(a) "Fast" RNG (Left) and Chien $K - \epsilon$ (b) "Mixing" RNG (Left) and Chien $K - \epsilon$

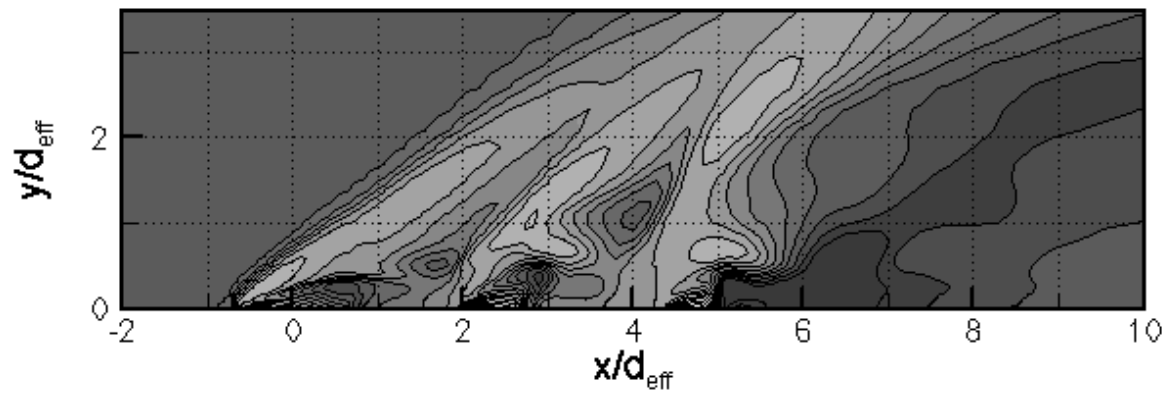
Figure 6.7. Helium Mass-Fraction Contours for Three Turbulence Models on a Spanwise Plane at $x/d_{eff} = 43.0$ (Measurement Plane) for the Nine-Hole Injector Array.



(a) Chien $K - \epsilon$

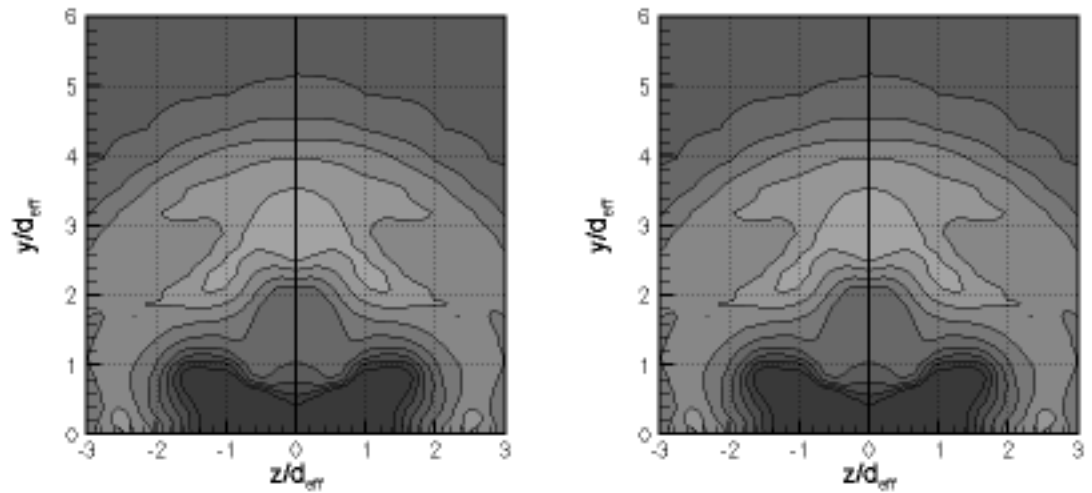


(b) "Fast" RNGK $-\epsilon$



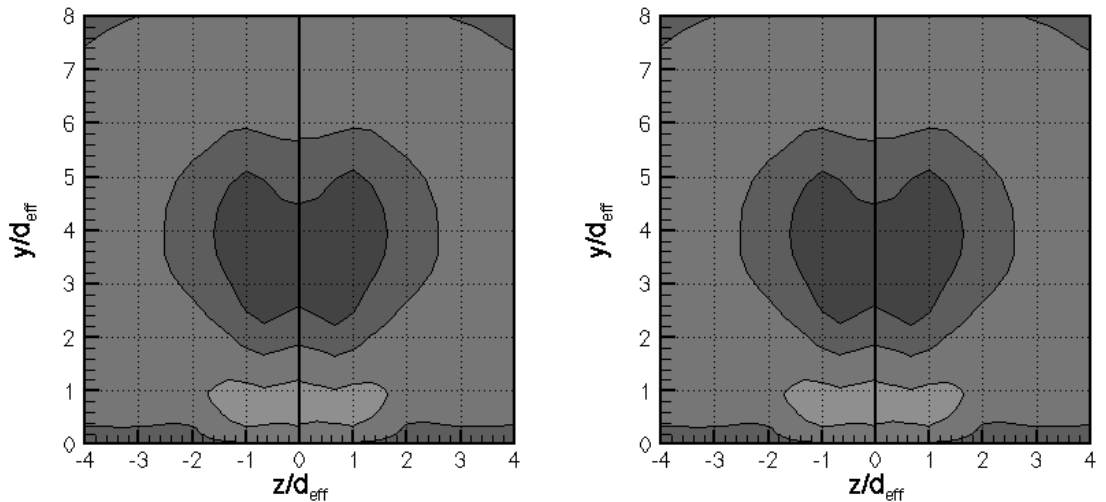
(c) "Mixing" RNGK $-\epsilon$

Figure 6.8. Centerplane Pressure Contours for Three Turbulence Models for the Nine-Hole Injector Array.



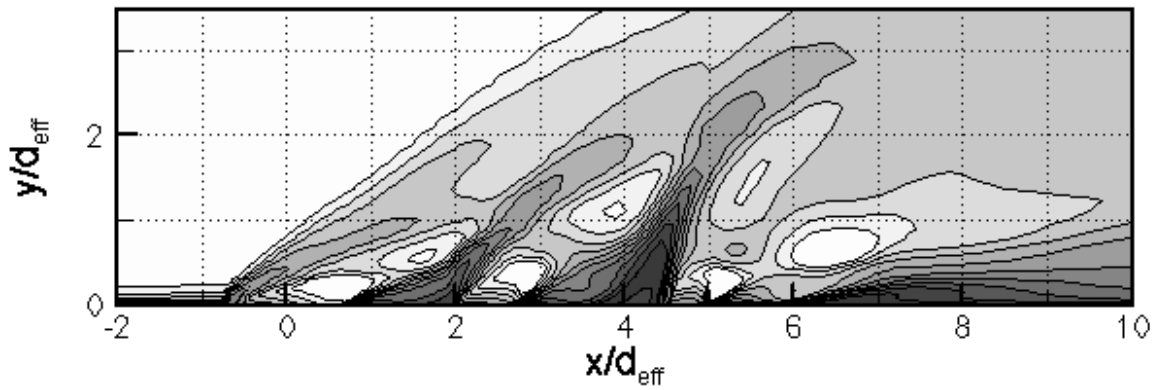
(a) "Fast" RNG (Left) and Chien $K - \epsilon$ (b) "Mixing" RNG (Left) and Chien $K - \epsilon$

Figure 6.9. Pressure Contours for Three Turbulence Models on a Spanwise Plane at $x/d_{\text{eff}} = 6.00$ for the Nine-Hole Injector Array.

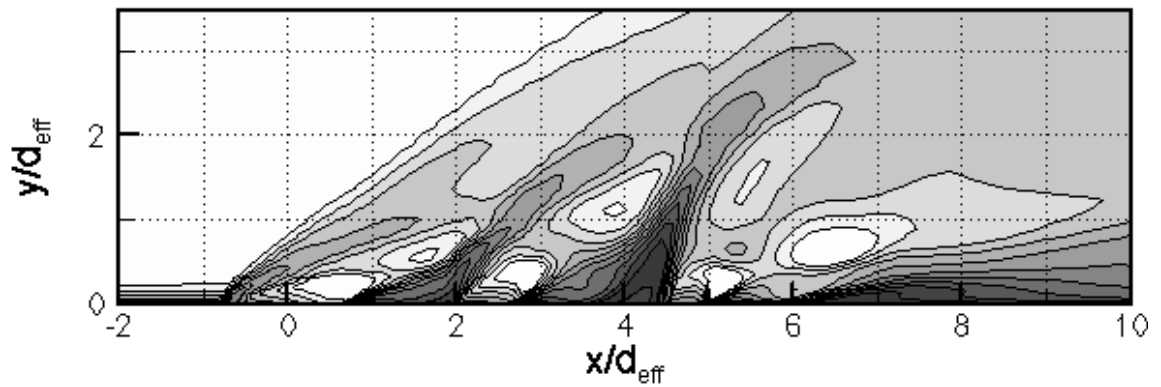


(a) "Fast" RNG (Left) and Chien $K - \epsilon$ (b) "Mixing" RNG (Left) and Chien $K - \epsilon$

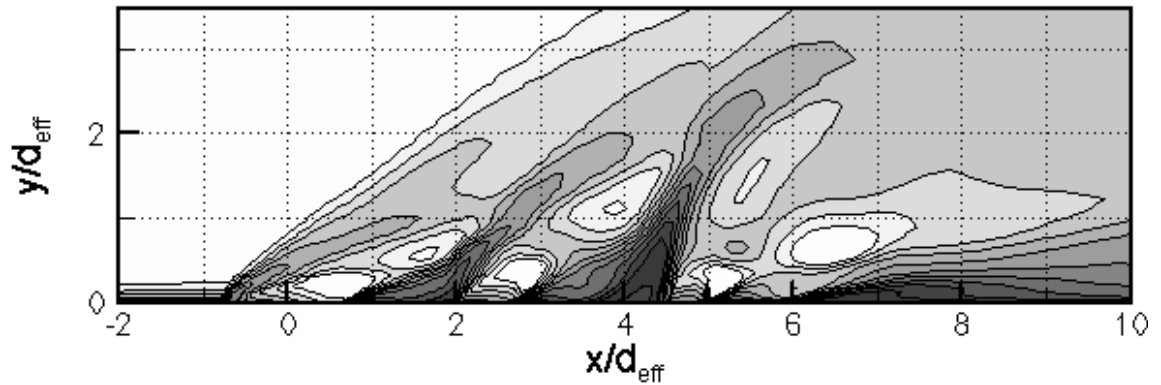
Figure 6.10. Pressure Contours for Three Turbulence Models on a Spanwise Plane at $x/d_{\text{eff}} = 43.0$ (Measurement Station) for the Nine-Hole Injector Array.



(a) Chien $K - \epsilon$

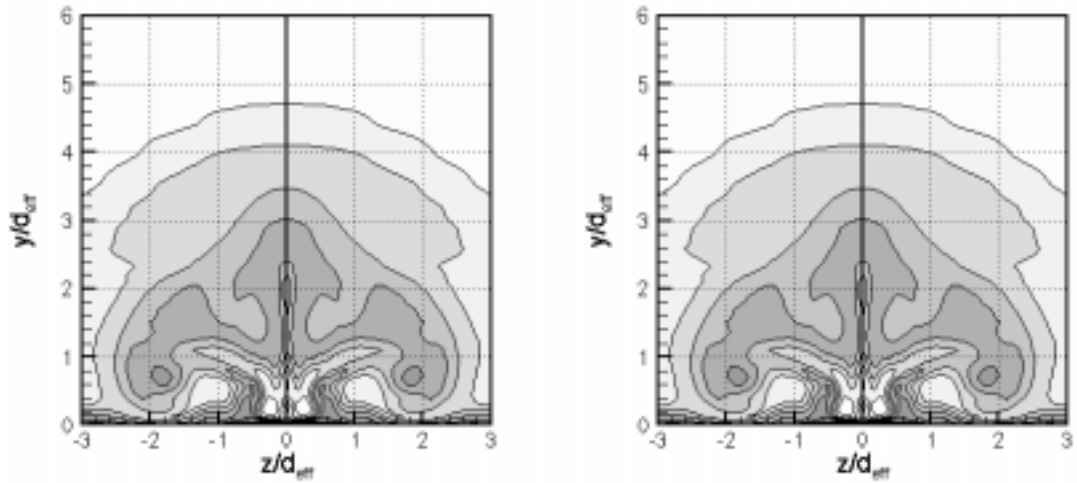


(b) "Fast" RNGK $-\epsilon$



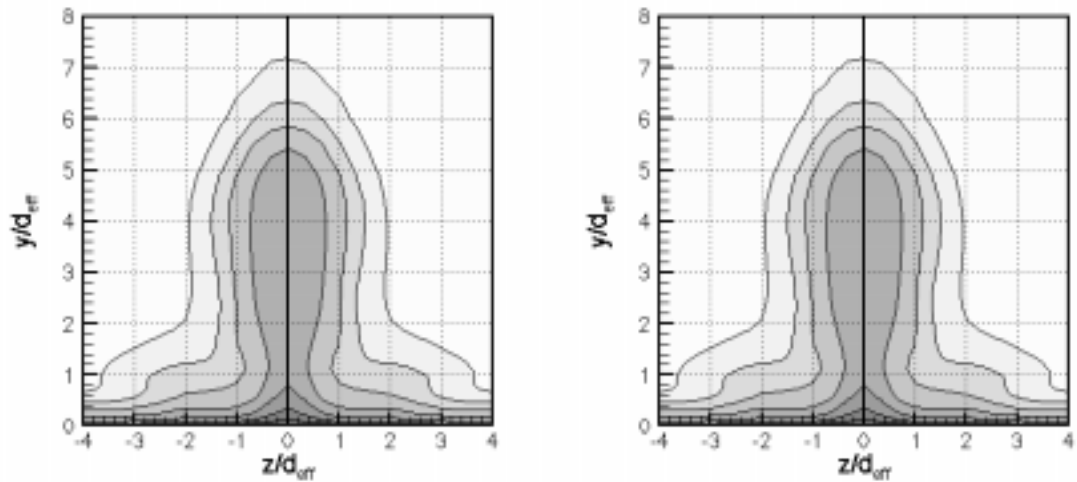
(c) "Mixing" RNGK $-\epsilon$

Figure 6.11. Centerplane Mach Contours for Three Turbulence Models for the Nine-Hole Injector Array.



(a) "Fast" RNG (Left) and Chien $K - \epsilon$ (b) "Mixing" RNG (Left) and Chien $K - \epsilon$

Figure 6.12. Mach Number Contours for Three Turbulence Models on a Spanwise Plane at $x/d_{eff} = 6.00$ for the Nine-Hole Injector Array.



(a) "Fast" RNG (Left) and Chien $K - \epsilon$ (b) "Mixing" RNG (Left) and Chien $K - \epsilon$

Figure 6.13. Mach Number Contours for Three Turbulence Models on a Spanwise Plane at $x/d_{eff} = 43.0$ for the Nine-Hole Injector Array.